

Hidden-Rashba-driven Absence of Odd-integer Quantized States in an Oxide Quantum Hall System

Jingyue Wang^{1†}, Junwei Huang^{2†}, Daniel Kaplan^{3†}, Xuehan Zhou^{1†}, Congwei Tan^{1†}, Jing Zhang⁴, Gangjian Jin⁴, Xuzhong Cong¹, Yongchao Zhu¹, Xiaoyin Gao¹, Yan Liang¹, Huakun Zuo⁴, Zengwei Zhu⁴, Ruixue Zhu⁵, Ady Stern³, Hongtao Liu¹, Peng Gao⁵, Binghai Yan^{3*}, Hongtao Yuan^{2*}, Hailin Peng^{1*}

¹ Center for Nanochemistry, Beijing Science and Engineering Center for Nanocarbons, Beijing National Laboratory for Molecular Sciences, College of Chemistry and Molecular Engineering, Peking University, 100871, Beijing, China.

² National Laboratory of Solid State Microstructures, Collaborative Innovation Center of Advanced Microstructures, College of Engineering and Applied Sciences, and Jiangsu Key Laboratory of Artificial Functional Materials, Nanjing University, 210000, Nanjing, China.

³ Department of Condensed Matter Physics, Weizmann Institute of Science, 7610001, Rehovot, Israel.

⁴ Wuhan National High Magnetic Field Center and School of Physics, Huazhong University of Science and Technology, 430074, Wuhan, China.

⁵ International Center for Quantum Materials and Electron Microscopy Laboratory, School of Physics, Peking University, 100871, Beijing, China.

† These authors contributed equally to this work.

*Corresponding author. E-mail: hlpeng@pku.edu.cn, htyuan@nju.edu.cn, binghai.yan@weizmann.ac.il

Abstract:

The discovery of the quantum Hall effect in 1980, a turning point in condensed matter physics, has inspired exploring emergent quantized states regarding novel electron states, band topologies and spin textures. Owing to the lifted degeneracies universally-existing, most quantum Hall systems host both even- and odd-integer quantum Hall plateaus simultaneously. Selective control of these quantized states is of great significance to understand the exotic ground states and manipulate the

spin textures in quantum Hall systems; however, it remains challenging. Here we demonstrate the absence of odd-integer state in inversion-symmetric $\text{Bi}_2\text{O}_2\text{Se}$ quantum Hall system driven by the unique hidden Rashba effect. Pronounced quantum oscillations and only even-integer quantized plateaus were observed in the few-layer $\text{Bi}_2\text{O}_2\text{Se}$ films epitaxially grown on SrTiO_3 . However, after reducing the thickness of epitaxial $\text{Bi}_2\text{O}_2\text{Se}$ film to one unit cell limit with giant Rashba parameter of $440 \text{ meV}\cdot\text{\AA}$, both odd- and even-integer states can show up simultaneously in this 2D Janus film. Theoretical calculations revealed that such absence of odd-integer states, i.e., a suppressed Zeeman splitting, stems from a unique hidden Rashba effect in the inversion-symmetric $\text{Bi}_2\text{O}_2\text{Se}$. However, this hidden Rashba effect can be further broken down due to tunable inversion-symmetry breaking. Our work highlights the extraordinary controllability of quantized states at the atomic level and further provides an unprecedented path to explore and handle novel spin textures and ground states.

Main Text:

The quantum Hall effect (QHE) is of great significance for probing and understanding novel electron states in two-dimensional (2D) systems¹⁻¹⁴. In the integer QHE, the Hall resistance, which is the transverse voltage of the device divided by the longitudinal current, is quantized into plateaus of height h/ve^2 , where h is Planck's constant, e is the electron's charge, and v is an integer. In most 2D electronic systems, the coexistence of even- and odd-integer quantum Hall plateaus can be universally observed^{2,5,7,9-13,15-19}, since when the magnetic field $B \geq 30 \text{ T}$, the Zeeman splitting energy reaches 3.5 meV (if the g factor around 2), which is much larger than thermal (0.36 meV for 4.2 K) and Dingle (0.86 meV for Dingle temperature of 10 K) broadening energies. The similar QHE in these systems indicate the same spin textures with lifted spin degeneracies. Recently, the emergence of 2D layered materials has provided unprecedented opportunities to explore unique spin textures and QHE in the 2D limit, when the electron states and spin textures can be tuned by external modulation of electric field and by the inversion-symmetry engineering at the atomic level^{3,4,7,9,13-16,18-21}. However, in the previously reported QHE in 2D layered materials, the quantization in a high magnetic field is mainly prevailed by the Zeeman effect, whereas spin-orbital coupling (SOC) is negligible due to the light atomic weight of conducting atoms. Thus, it is of great significance to achieve new spin textures and to tailor the QHE in a heavy quantum Hall system when SOC dominates the electron states, for instance, the absence of odd-integer quantum Hall states with degenerated spin textures. Furthermore, the regulation of unique spin textures in heavy

systems will also provide a new route for understanding the SOC-related physics and exploring potential spintronic applications.

In this work, we demonstrate the absence of odd-integer state when the magnetic field exceeds 50 T in inversion-symmetric $\text{Bi}_2\text{O}_2\text{Se}$ quantum Hall system driven by a unique spin-degenerated Rashba bilayer structure and hidden Rashba effect²². These unusual quantum Hall states can be regulated via thickness control. Both odd- and even-integer quantum Hall plateaus appear when the film thickness reduces to 1 unit cell (uc, 1-uc-thick $\text{Bi}_2\text{O}_2\text{Se}$ contains 2 layers), where interface-induced inversion-symmetry breaking changes the spin degeneracy of electrons due to a giant conventional Rashba effect. The Rashba parameter α_R^0 in this 2D Janus structure reaches $440 \text{ meV}\cdot\text{\AA}$, which is one of the largest values among the known 2D semiconducting Rashba systems. Different types of Rashba effects and QHE can be effectively tailored by inversion-symmetry engineering in high-mobility 2D $\text{Bi}_2\text{O}_2\text{Se}$ films, providing a new platform to control novel electron states, band topologies and spin textures. Therefore, our work offers extraordinary opportunities to manipulate the electron's spin and will shed light on new physics and applications in electronics and spintronics.

Crystal structure and hidden Rashba effect in layered $\text{Bi}_2\text{O}_2\text{Se}$

We choose 2D $\text{Bi}_2\text{O}_2\text{Se}$ as the target material because of the following unique characteristics. Firstly, the electron states near the conduction band minimum originate mainly from the heavy Bi p -orbital bands with strong SOC. Thus, 2D $\text{Bi}_2\text{O}_2\text{Se}$ can serve as an ideal platform to study and tailor SOC and spin textures. Secondly, different from van der Waals materials, bulk $\text{Bi}_2\text{O}_2\text{Se}$ shows an inversion-symmetric layered lattice structure with tetragonal $[\text{Bi}_2\text{O}_2]^{2+}$ layers and $[\text{Se}]^{2-}$ layers alternately stacked along the c axis, forming unique inter-layer dipoles²³⁻²⁵ (Fig. 1a). For the $[\text{Bi}_2\text{O}_2]^{2+}$ layer consisting of one O layer sandwiched by two Bi monolayers with the dipole and strong atomic SOC, each Bi monolayer feels a strong Rashba effect while neighboring Bi monolayers exhibit opposite signs of Rashba SOC. Consequently, each $[\text{Bi}_2\text{O}_2]^{2+}$ layer forms a Rashba bilayer (Fig. 1b), in which the bands are spin-degenerated and the total Rashba spin texture is hidden in the presence of inversion symmetry²². Different from the conventional inversion-symmetry breaking induced Rashba effect^{14,26-31}, the hidden Rashba effect has not been studied in the quantum Hall regime before and will result in unique QHE due to the coupling of opposite SOC layers (Fig. 1c). Thirdly, the hidden Rashba effect can be regulated via thickness control, and

high-mobility Bi₂O₂Se films can be controllably grown by the molecular beam epitaxy (MBE) technique (see Materials and Methods) with different thicknesses even down to 1 uc (Fig. S1)^{32,33}. In the presence of the substrate, the inversion symmetry will change in epitaxial films with various thicknesses. As shown in Fig. 1d, the interfacial Bi₂O₂Se layer is inversion-asymmetric and forms a Janus structure due to the giant dielectric-constant difference and absence of bottom Se atom at the interface. In contrast, the Bi₂O₂Se layers away from the interface are inversion-symmetric. Consequently, the thick epitaxial Bi₂O₂Se films almost preserve inversion symmetry and exhibit hidden Rashba effect, while the thin films will show giant inversion asymmetry and conventional Rashba effect. Thus, the high-mobility epitaxial 2D Bi₂O₂Se films with tunable thicknesses enable the selective control of inversion symmetry, spin textures and quantum Hall states.

To demonstrate the excellent mobility property in epitaxial Bi₂O₂Se films, we performed low-temperature Hall effect measurements (Fig. 1e), based on which the Hall mobility ($\mu_{\text{Hall}} = \sigma/n_{\text{H}}e$, where σ is the sheet conductance, n_{H} is the sheet carrier density extracted from the Hall measurements) can be obtained. Three significant observations need to be addressed here. Firstly, the Hall mobility of epitaxial Bi₂O₂Se films at lowest temperature reaches a maximum value of 12,435 cm²·V⁻¹·s⁻¹, which enables us to observe Shubnikov–de Haas (SdH) oscillations and quantized states therein. Secondly, the Hall mobility increases with increasing thickness. The decrease of carrier mobility in the ultrathin Bi₂O₂Se film is presumably due to the scatterings from the interface and the top surface. Thirdly, the mobility in non-encapsulated Bi₂O₂Se films is higher than that in other reported non-encapsulated 2D semiconductors^{13,17,34-36} due to the small effective mass, the excellent chemical stability in ambient conditions and the high-quality crystalline order of the epitaxial Bi₂O₂Se films (Table. S1). The nature of ultrahigh mobility makes 2D Bi₂O₂Se an excellent material platform to study SdH oscillations and QHE.

SdH oscillations and QHE in 2D Bi₂O₂Se with various thicknesses

The angular-dependent magnetoresistance measurements were performed to confirm the 2D nature of the epitaxial films. As shown in Fig. 2a, we observed pronounced SdH oscillations in the longitudinal magnetoresistance R_{xx} in the 6-uc-thick epitaxial Bi₂O₂Se film when applying static magnetic fields (B) up to 14 T. The positions of the SdH oscillation extrema as a function of the perpendicular component of the field barely move when tilting the angle (θ) between the magnetic field and the normal direction of the sample plane, indicating a 2D feature of the 6-uc-thick

Bi₂O₂Se (Fig. 2a) with a single frequency (Fig. S2a). Meanwhile, the angle-dependent oscillation frequency f extracted from the fast Fourier transform (FFT) analysis can be well fitted by a 2D model ($f \propto 1/\cos\theta$), also revealing a strict 2D Fermi surface in the Bi₂O₂Se film (Fig. S2b). Note that the absence of Zeeman splitting induced Landau level (LL) crossing within the experimental maximum B of 14 T indicates a small effective Landé g -factor in the 6-uc-thick device ^{7,14}.

Figure 2b shows the quantized states of the Hall resistance (R_{xy}) in the 6-uc-thick epitaxial Bi₂O₂Se at 4.2 K in pulsed high magnetic field up to 50 T ^{37,38}. Remarkably, only even-integer quantum Hall plateaus ($\nu = 2, 4, 6, \dots$) were clearly observed when tuning the carrier densities through the SrTiO₃ (STO) dielectric substrate (Fig. S3 and S4). Similar even-integer QHE was observed in the static magnetic fields at 1.5 K (Fig. S5). To confirm the intrinsic and robust nature of the missing odd-integer quantum Hall plateaus in 2D Bi₂O₂Se systems, free-standing nanosheet of Bi₂O₂Se ³⁹ with thickness up to 9 uc were grown via chemical vapor deposition (CVD) and transferred as van der Waals stacked 2D Hall devices for the electronical measurements. The atomically-flat and high- κ 2D layered Bi₂SeO₅ dielectric notably improved the mobility of 2D Bi₂O₂Se nanosheet ⁴⁰. As shown in Fig. 2c and 2d, only even-integer quantum Hall plateaus ($\nu = 2, 4, 6, 8, 10, \dots$) in inversion-symmetric Bi₂O₂Se nanosheet clearly emerge down to the quantum limit with filling factor $\nu = 2$ as the magnetic field increases. This is similar to that the observations in the 6-uc-thick epitaxial film.

We then studied the thickness-dependent evolutions of SdH oscillations and QHE in epitaxial Bi₂O₂Se films. As shown in Fig. 3a and 3b, the R_{xx} - B and R_{xy} - B measurements of the 6-uc-thick and 2.5-uc-thick Bi₂O₂Se films under pulsed magnetic fields up to 50 and 55 T were performed, respectively. Note that only even-integer quantum Hall plateaus, i.e., $\nu = 2, 4, 6, 8, 10, 12, \dots$, can be observed (Fig. 3a, 3b, Fig. S6a and Fig. S7a). Meanwhile, the consistent QHE in 6- and 2.5-uc-thick films excludes the existence of parallel, independent QHE layers, which is a trivial explanation of the missing of odd-integer quantum Hall states. Otherwise, the plateau step would be proportional to the film thickness. In the 6-uc-thick device, R_{xx} exhibits a strict zero plateau when the magnetic field exceed 42 T, revealing a strict QHE therein. In the 2.5-uc-thick device, R_{xx} almost reaches zero when magnetic field $B = 50$ T. When the film thickness was further reduced to 1 uc, significant SdH oscillations and quantized plateaus can still be observed. Surprisingly, both odd- and even-integer quantum Hall plateaus appeared in the 1-uc-thick device. As shown in Fig. 3c, an odd-integer quantum Hall plateau of $\nu = 5$ appeared at $B > 40$ T, which is totally

different from the absence of odd-integer QHE in thicker films. Meanwhile, two valleys ($\nu = 6$ and $\nu = 7$) between the $\nu = 5$ and $\nu = 8$ plateaus in R_{xx} - B curves can be observed clearly, indicating the fully separation of spin polarizations under high magnetic fields. The coexistence of odd- and even- integer quantum Hall states can also be observed when tuning the carrier density in this device (Fig. S6b and Fig. S7b).

Analysis of quantum oscillations in 2D Bi₂O₂Se with various thicknesses

We firstly performed FFT analysis of quantum oscillations in R_{xx} , from which information about the 2D Fermi surfaces can be extracted (Fig. 3d). For the 6-uc-thick device, the quantum oscillations exhibit single frequency (f) as shown in top panel in Fig. 3d, revealing negligible spin splitting. The absence of splitting in the FFT spectrum indicates inversion-symmetric band structure in the 6-uc-thick device. For the 2.5-uc-thick device, the quantum oscillations show minor splitting ($\Delta f = 11$ T) in the FFT spectrum. The splitting behavior may arise from the formation of inner-outer Fermi surfaces and indicates a minor symmetry breaking. In contrast, for the 1-uc-thick device, the quantum oscillations show a distinct beating behavior of $\Delta f > 60$ T, suggesting two distinct bands therein.

Landau fan diagrams were further performed to confirm the spin degeneracies in epitaxial Bi₂O₂Se films. The slopes (k) in the Landau fan diagram correspond to the carrier densities of bands ($n_{2D} = s \times k \times e/h$, where n_{2D} is the carrier density, s is the spin degeneracy). In the 6-uc-thick film, the slope in Landau fan diagram is 49.4 T (Fig. 3e), which correspond to carrier densities of $s \times 1.2 \times 10^{12}$ cm⁻², respectively. Meanwhile, the carrier densities obtained from the Hall curves are 2.6×10^{12} cm⁻². Thus, by comparing the carrier densities obtained from the two different methods, we confirmed the spin degeneracy $s = 2$ in the 6-uc-thick film without any signature of Zeeman splitting, which is the same as that in the 2.5-uc-thick film (carrier densities extracted from the Landau plot and the Hall curve are $s \times 3.8 \times 10^{12}$ cm⁻² and 7.1×10^{12} cm⁻²). Such absence of Zeeman splitting indicates that the energy gap is smaller than thermal broadening, $(g\mu_B B - \Gamma)/2 < k_B T$ ⁹, where μ_B and k_B stand for Bohr magneton and Boltzmann constant, respectively, $\Gamma (= \pi k_B T_D)$ stands for the disorder broadening of LLs, and T_D represents the Dingle temperature of ~ 10 K (Fig. S8 to S10). At magnetic fields higher than 50 T, the absence of an observable Zeeman splitting suggests that the effective g -factor of Bi₂O₂Se is smaller than 1.28. This is significantly different

from other 2D semiconductors such as black phosphorus, InSe and transition metal dichalcogenides ^{7,9-11} (Table S2).

By applying FFT and inverse FFT analyses of quantum oscillations in the 1-uc-thick device (Fig. S11), we conducted the Landau fan diagram of the two splitting peaks in the FFT spectrum. As shown in Fig. 3g, the carrier densities extracted from the slopes of Landau fans are $s \times 2.1 \times 10^{12} \text{ cm}^{-2}$ and $s \times 3.5 \times 10^{12} \text{ cm}^{-2}$. By comparing the carrier density extracted from the Hall curve, $6.0 \times 10^{12} \text{ cm}^{-2}$, we found that the spin degeneracies of two splitting peaks are $s = 1$, and thus the splitting in the FFT spectrum arises from the global Rashba splitting in the 1-uc-thick film. Therefore, the $\nu = 5$ quantum Hall plateau in the 1-uc-thick film is contributed by the inner ($\nu = 2$) and outer ($\nu = 3$) Rashba pockets (Fig. S11). The global Rashba parameter exhibits a large value of $\alpha_R^0 \approx \frac{\hbar^2}{m^*} \sqrt{\frac{\pi}{2}} \frac{\Delta n}{\sqrt{n}} \approx 440 \text{ meV} \cdot \text{\AA}$ therein, where \hbar is reduced Planck constant, m^* is the effective mass, Δn is the difference in densities between majority and minority spin carriers ³⁰. The energy difference $\Delta E = 2\Delta k \alpha_R^0$ between band minimums of inner and outer pockets in the 1-uc-thick device reaches 14.3 meV. The giant conventional Rashba splitting in ultrathin Bi₂O₂Se film indicates significant inversion-symmetry breaking therein. As applying a large gate voltage will change the inversion symmetry and the Rashba parameters, all the quantum transport measurements were performed without applying a gate voltage in this figure. The analysis of quantum oscillations clearly reveals that the various quantum Hall states appearing in the Bi₂O₂Se films are related to different spin degeneracies and inversion symmetries. Note that epitaxial 1-uc-thick Bi₂O₂Se has one of the strongest Rashba splitting among known Rashba systems as summarized in Table S3 ^{14,28,30,41-46}, thus can serve as an ideal platform for studying Rashba-related physics such as intrinsic spin Hall effect ^{47,48}, spin interference ⁴⁹, spin galvanic effect ⁵⁰, and spin-orbital torque ^{51,52}.

Theoretical model for the origin of unique QHE

We adopt a Rashba bilayer model based on *ab initio* band structures of Bi₂O₂Se thin films to understand the absence of odd-integer quantum Hall plateaus in 2D Bi₂O₂Se (Fig. S12 to S16). A Bi₂O₂Se film with n uc thick has $4n$ Rashba layers, as shown in Fig. 4a. Note that Rashba monolayers couple strongly inside a [Bi₂O₂]²⁺ layer but weakly between neighboring [Bi₂O₂]²⁺ layers. The interlayer coupling alternates along the z direction like a Su–Schrieffer–Heeger chain ⁵³, as shown in Fig. 4a. Because of the considerable difference between intra- and inter-layer

coupling, we can further downfold the low energy states to $2n$ Rashba layers. In such an effective model, neighboring Rashba layers exhibit opposite Rashba coefficients ($\pm\alpha$) but uniform interlayer coupling (t). Note that the Rashba parameter α originates from the Rashba monolayer in each $[\text{Bi}_2\text{O}_2]^{2+}$ layers, and is different from the global Rashba parameter α_R^0 in Figure 3. As we will show in the following, the hidden Rashba effect will dramatically suppress the Zeeman splitting in the QHE.

The effective Hamiltonian for a n -uc-thick film is,

$$H = \frac{p^2}{2m^*} \delta_{l,l'} + (-1)^l \alpha (k_y \sigma_x - k_x \sigma_y) / \hbar - t \delta_{l,l\pm 1} \delta_{\sigma\sigma'}. \quad (1)$$

Where m^* is the effective mass, $p^2 = p_x^2 + p_y^2$ are the in-plane momentum, $\sigma_{x,y}$ are Pauli matrices which denote the spin degree of freedom, $l=1,2,3,\dots,2n$ is the Rashba layer index and $(-1)^l \alpha$ represents the alternating Rashba layers. This model respects both inversion symmetry and time-reversal symmetry and thus gives doubly degenerate bands. The lowest band corresponds to the Fermi surface observed in our experiments. We carried out *ab initio* calculations on $\text{Bi}_2\text{O}_2\text{Se}$ films of different thicknesses and extracted parameters for Eq. (1), $m^* = 0.14 m_0$, $t = 0.2$ eV and $\alpha = 1.45$ eV \cdot Å. In addition, for the film with $(n + 1/2)$ uc thick, we can build a similar $2n$ Rashba layer model with slightly modified parameters (Section 9.3 in SI).

The magnetic field (B) is treated in the Landau gauge by considering the replacement $p \rightarrow p + eA$ (for electrons) with $A = (0, Bx, 0)$. For multiple Rashba layers, the coupling matrix between n and m LLs reads,

$$H_{nm}^{l,l'} = \hbar\omega_c \left(n + \frac{1}{2} \right) \delta_{nm} \delta_{ll'} - t \delta_{nm} \delta_{l,l'\pm 1} + \frac{g_0 \mu_B B \sigma_z}{2} \delta_{nm} + \frac{(-1)^l \sqrt{2} \alpha}{l_B} (\delta_{n,m+1} \sigma^+ + \delta_{n,m-1} \sigma^-). \quad (2)$$

Here, $\omega_c = eB/m^*$, $l_B = \sqrt{\hbar/eB}$ are the cyclotron frequency and magnetic length, respectively, $g_0 \approx 2$ is the bare Landé g -factor, and $\sigma^\pm = (\sigma_x \pm i\sigma_y)/2$. The Landau-quantized momentum operators renormalize the Rashba interaction such that it couples different LLs and thus competes with the bare Zeeman splitting [third term in Eq. (2)], due to the ladder structure of momentum operators [the fourth term in Eq. (2)]. The induced splitting between (n, σ) and (n, σ') LLs represents the effective Zeeman energy (E_Z). One can verify $E_Z = g_0 \mu_B B$ at $\alpha = 0$ and find that E_Z decreases from $g_0 \mu_B B$ to zero and further to a negative value with increasing α .

The effective g -factors $g_{eff} = |\Delta\varepsilon/\mu_B B|$ of $\text{Bi}_2\text{O}_2\text{Se}$ films will be dramatically suppressed in the inversion-symmetric scenario. Figure 4b shows the g_{eff} in dependence of α for the 6-uc-thick epitaxial $\text{Bi}_2\text{O}_2\text{Se}$ films, whose band structure is plotted in Fig. 4c. For the n -th LL, g_{eff} first decreases from g_0 to zero and further increases with increasing Rashba α . From the calculated Landau fan diagram (Fig. S20), increasing α pushes the upper Zeeman split LL down toward the lower LL and eventually switch their order, leading to g_{eff} trend observed. At the material parameter region of α , the small g_{eff} satisfies the experimental requirement for $n \leq 4$ ($g_{eff} < 1.28$) to suppress the odd-integer Hall plateaus when the films preserve inversion symmetry. Figure 4d and 4e exhibits the g_{eff} and band structure of the 2.5-uc-thick film, which almost preserves inversion symmetry. Similar to that in the 6-uc-thick film, the small g_{eff} in the 2.5-uc-thick film also satisfies the experimental requirement for $n \leq 4$ ($g_{eff} < 1.28$) to suppress the odd-integer Hall plateaus. Furthermore, we will provide a vivid description of the suppression of Zeeman splitting due to hidden Rashba effect. In the relevant small α region (compared to t), a naive picture is that the Rashba SOC forces spins to orient in the basal plane and suppresses the bare Zeeman effect which tends to align spins along the z -axis. In the larger α region, the subtle balance between α and t determines the effective Zeeman energy. In the single Rashba bilayer model, a flat band dispersion emerges when $t = (\alpha/\hbar)^2 m^*$ (Fig. S19). Here, the flat-band density of states exhibits a power-law ($\varepsilon^{-1/2}$) divergence because of the high-order dispersion ($\varepsilon \sim k^4$) near the band edge.

As shown in Fig. S20a, the 1-uc-thick film would present negligible Zeeman splitting in experiment if the inversion symmetry is preserved. However, the Rashba bilayer scenario breaks down if the inversion symmetry is strongly violated (Fig. S21 and S22), for example, by the presence of substrate. The origin of thickness-dependent global Rashba effect is summarized in Section 11 in SI. For the 1-uc-thick film, we introduce a symmetry breaking term $\Delta\tau_z$ in Eq. (1), where τ_z is the Pauli matrix for the layer degree of freedom and $\Delta = 78$ meV, to reproduce the conventional Rashba splitting observed in experiments. As shown in Fig. 4f, g_{eff} is still suppressed in the small α region, soon passes the critical point and increases to a large value for the realistic α (the vertical dashed line) in the inversion-asymmetric film (Fig. 4g). Consequently, we obtain quite large g_{eff} in calculations (Fig. 4f, and S22), rationalizing the appearance of both even and odd plateaus in the quantum Hall regime. Thus, we verify that the even-integer QHE is

highly likely induced by the hidden Rashba effect, and the even-integer QHE vanishes when breaking the material inversion symmetry in theoretical calculations (summarized in Section 12 in SI), which is consistent with the tunable QHE as exhibited in Figure 3.

Conclusion

In summary, we demonstrated the experimental observation of the absence of odd-integer quantum Hall states originating from the unique degenerated Rashba bilayer structure and hidden Rashba effect in 2D Bi₂O₂Se films. The quantum Hall states in layered 2D Bi₂O₂Se can be selectively controlled via inversion-symmetry engineering at atomic level. In the 1-uc-thick Janus Bi₂O₂Se film, inversion-symmetry breaking brings out a giant conventional Rashba splitting of $\alpha_R^0 \approx 440$ meV·Å, which is one of the largest values among the known 2D semiconducting Rashba systems. The giant conventional Rashba effect changes the degeneracy of electrons and results in the coexistence of both odd- and even- integer quantum Hall states. Thus, the 2D Bi₂O₂Se system with strong and controllable SOC could open a new avenue to probe and tailor the spin textures as well as the quantum Hall states via inversion-symmetry engineering. In particular, the high mobility, as well as the strong and tunable SOC, make Bi₂O₂Se a promising candidate for realizing novel SOC-related phenomena, future logic devices and next-generation spintronic applications.

Materials and Methods

Bi₂O₂Se film growth and characterization

The Bi₂O₂Se films were grown in a homemade oxide molecular beam epitaxy (OMBE) system with base pressure better than 5×10^{-10} mbar. Firstly, the SrTiO₃ (STO) substrate was pretreated in ultrahigh vacuum (UHV) at 950 °C for 45 min to obtain single TiO₂-terminated surface. Then the substrate was annealed at 600 °C under the oxygen pressure of 1.3×10^{-4} mbar for 15 min to eliminate oxygen vacancies formed in the first step. After that the Bi₂O₂Se film was grown by co-evaporating Bi and Se precursors under the above oxygen pressure with substrate temperature keeping at 380 °C. The Bi source was set at 610 °C with a flux of ~ 0.75 Å/min and the Se source was set at 80 °C. To stop the growth, the shutters of Bi and Se sources were closed simultaneously and the sample was naturally cooled to room temperature. A step-climbing epitaxy growth mode occurs when the Bi₂O₂Se film is grown on stepped STO substrate, in which the n -th ($n = 1, 2, 3 \dots$) epilayer climbs the step with height difference from out-of-plane lattice mismatch and continues to grow the $n+1$ -th epilayer³³.

A Bruker Nanoscope system (Dimension Icon) with ScanAsyst mode was used to obtain the atomic force microscopy (AFM) images. The X-ray diffraction (XRD) measurements were performed with a Rigaku SmartLab (9 kW) X-ray diffractometer with a Ge (220) \times 2 crystal monochromator. The atomic resolution scanning transition electron microscopy (STEM) was performed on an aberration-corrected transmission electron microscope FEI Titan Cubed Themis G2 at 300 kV.

Fabrication of Hall devices

The Hall devices were fabricated directly on Bi₂O₂Se films grown on insulating STO substrates without encapsulation. We firstly patterned the MBE-grown Bi₂O₂Se films into discrete 40 \times 20 μm^2 rectangles by maskless laser direct writing (MLDW) and wet chemical etching (WCE) method⁵⁴. The MLDW instrument used was Heidelberg MLA150. The etchant is dilute H₂O₂ and protonic mixture acid (H₂SO₄: H₂O₂: H₂O=1: 2: 4). Secondly, alignment marker arrays were predefined onto the STO with standard photolithography technique. The photolithography instrument used was SUSS MA6 Gen4. Then Hall bar patterns can be obtained by standard electron beam lithography (EBL) and WCE with polymethyl methacrylate (PMMA) mask. Finally, EBL (FEI Quanta 250FEG equipped with Raith ELPHY Quantum) was used to fabricate multiple metal contacts for six-terminal Hall-bar structures. Ohmic contact was formed using Pd/Au metal electrodes (7 nm/45 nm) by E-beam evaporation (DE400). In order to avoid the influence from the substrate steps, all the devices were fabricated on individual terraces with the device channels parallel to the steps. The width of Hall bar ranges from 1.5 to 3 microns, the length of the channel ranges from 5 to 10 microns.

The fabrication process of Hall device of free-standing Bi₂O₂Se nanoplate is as follows: Bi₂O₂Se nanoplate was transferred on pre-exfoliated high- κ van der Waals layered Bi₂SeO₅ nanoplate with graphite back gate. Then, EBL and E-beam evaporation were used to prepare multiple metal contacts for six-terminal Hall-bar structures. The high- κ dielectric Bi₂SeO₅ isolated the roughness and Coulomb's scattering from SiO₂ substrate, thus enables the observation of QHE under a low magnetic field.

Electrical transport measurements

Electrical transport measurements were carried out in the following systems: an integrated cryofree static superconducting magnet system (14-T TeslatronPT from Oxford Instruments, or 9-T

AttoDry2100 from Attocube Systems), and the pulsed high magnetic field facility (55 T) at Wuhan National High Magnetic Field Center. An *in-situ* annealing process was necessary before the electrical transport measurements. Namely, the sample was mounted into the chamber, and then pumped to a high vacuum better than 10^{-3} mbar and heated to 385 K. The sample was kept at above conditions for about 1 hour, and the resistance was decreased rapidly to a constant value. Subsequently, the sample was cooled down to the base temperature of the cryogenic systems. The gate voltage was applied by Keithley 2400 on the Bi₂O₂Se devices with STO (001) or Bi₂SeO₅ as the gate dielectric. At static magnetic fields, the electrical transport signals were detected by using multiple lock-in amplifiers (Stanford Research Systems, SR830) with an AC excitation current (I) below 1 μ A at a frequency between 10 and 20 Hz. Under pulsed high magnetic fields, the Bi₂O₂Se devices were immersed into liquid helium to avoid eddy-current heating, and the electric resistance was measured by using a DC technique with a current of 2.5 μ A. Four pulsed shots for the magnetoresistance measurements at different conditions ($+I+B$, $+I-B$, $-I+B$, $-I-B$) were performed to obtain pure QHE signals. Results from different systems and different samples are reproducible and consistent.

Competing interests

Authors declare that they have no competing interests.

Data and materials availability

All data needed to evaluate the conclusions in this paper are present in the paper or the supplementary materials.

References

- 1 Klitzing, K. v., Dorda, G. & Pepper, M. New Method for High-Accuracy Determination of the Fine-Structure Constant Based on Quantized Hall Resistance. *Phys. Rev. Lett.* **45**, 494-497 (1980).
- 2 Tsui, D. C., Stormer, H. L. & Gossard, A. C. Two-Dimensional Magnetotransport in the Extreme Quantum Limit. *Phys. Rev. Lett.* **48**, 1559-1562 (1982).
- 3 Novoselov, K. S. *et al.* Two-dimensional gas of massless Dirac fermions in graphene. *Nature* **438**, 197-200 (2005).

- 4 Zhang, Y., Tan, Y.-W., Stormer, H. L. & Kim, P. Experimental observation of the quantum Hall effect and Berry's phase in graphene. *Nature* **438**, 201-204 (2005).
- 5 Tsukazaki, A. *et al.* Quantum Hall Effect in Polar Oxide Heterostructures. *Science* **315**, 1388-1391 (2007).
- 6 Chang, C.-Z. *et al.* Experimental Observation of the Quantum Anomalous Hall Effect in a Magnetic Topological Insulator. *Science* **340**, 167-170 (2013).
- 7 Li, L. *et al.* Quantum Hall effect in black phosphorus two-dimensional electron system. *Nat. Nanotechnol.* **11**, 593-597 (2016).
- 8 Matsubara, Y. *et al.* Observation of the quantum Hall effect in δ -doped SrTiO₃. *Nat. Commun.* **7**, 11631 (2016).
- 9 Bandurin, D. A. *et al.* High electron mobility, quantum Hall effect and anomalous optical response in atomically thin InSe. *Nat. Nanotechnol.* **12**, 223-227 (2017).
- 10 Movva, H. C. P. *et al.* Density-Dependent Quantum Hall States and Zeeman Splitting in Monolayer and Bilayer WSe₂. *Phys. Rev. Lett.* **118**, 247701 (2017).
- 11 Xu, S. *et al.* Odd-Integer Quantum Hall States and Giant Spin Susceptibility in p-Type Few-Layer WSe₂. *Phys. Rev. Lett.* **118**, 067702 (2017).
- 12 Yang, J. *et al.* Integer and Fractional Quantum Hall effect in Ultrahigh Quality Few-layer Black Phosphorus Transistors. *Nano Lett.* **18**, 229-234 (2018).
- 13 Qiu, G. *et al.* Quantum Hall effect of Weyl fermions in n-type semiconducting tellurene. *Nat. Nanotechnol.* **15**, 585-591 (2020).
- 14 Sheng, F. *et al.* Rashba valleys and quantum Hall states in few-layer black arsenic. *Nature* **593**, 56-60 (2021).
- 15 Bolotin, K. I., Ghahari, F., Shulman, M. D., Stormer, H. L. & Kim, P. Observation of the fractional quantum Hall effect in graphene. *Nature* **462**, 196-199 (2009).
- 16 Du, X., Skachko, I., Duerr, F., Luican, A. & Andrei, E. Y. Fractional quantum Hall effect and insulating phase of Dirac electrons in graphene. *Nature* **462**, 192-195 (2009).
- 17 Li, L. *et al.* Quantum oscillations in a two-dimensional electron gas in black phosphorus thin films. *Nat. Nanotechnol.* **10**, 608-613 (2015).

- 18 Fallahazad, B. *et al.* Shubnikov--de Haas Oscillations of High-Mobility Holes in Monolayer and Bilayer WSe₂: Landau Level Degeneracy, Effective Mass, and Negative Compressibility. *Phys. Rev. Lett.* **116**, 086601 (2016).
- 19 Pisoni, R. *et al.* Interactions and Magnetotransport through Spin-Valley Coupled Landau Levels in Monolayer MoS₂. *Phys. Rev. Lett.* **121**, 247701 (2018).
- 20 Suzuki, R. *et al.* Valley-dependent spin polarization in bulk MoS₂ with broken inversion symmetry. *Nat. Nanotechnol.* **9**, 611-617 (2014).
- 21 Du, L. *et al.* Engineering symmetry breaking in 2D layered materials. *Nat. Rev. Phys.* **3**, 193-206 (2021).
- 22 Zhang, X., Liu, Q., Luo, J.-W., Freeman, A. J. & Zunger, A. Hidden spin polarization in inversion-symmetric bulk crystals. *Nat. Phys.* **10**, 387-393 (2014).
- 23 Wu, J. *et al.* High electron mobility and quantum oscillations in non-encapsulated ultrathin semiconducting Bi₂O₂Se. *Nat. Nanotechnol.* **12**, 530-534 (2017).
- 24 Wang, F. *et al.* Phonon signatures for polaron formation in an anharmonic semiconductor. *Proc. Nat. Acad. Sci.* **119**, e2122436119 (2022).
- 25 Tan, C. *et al.* 2D fin field-effect transistors integrated with epitaxial high-k gate oxide. *Nature* **616**, 66-72 (2023).
- 26 Yu, A. B. & Rashba, E. I. Oscillatory effects and the magnetic susceptibility of carriers in inversion layers. *J. Phys. C Solid State Phys.* **17**, 6039 (1984).
- 27 Luo, J., Munekata, H., Fang, F. F. & Stiles, P. J. Observation of the zero-field spin splitting of the ground electron subband in gasb-inas-gasb quantum wells. *Phys. Rev. B* **38**, 10142-10145 (1988).
- 28 Nitta, J., Akazaki, T., Takayanagi, H. & Enoki, T. Gate Control of Spin-Orbit Interaction in an Inverted In_{0.53}Ga_{0.47}As/In_{0.52}Al_{0.48}As Heterostructure. *Phys. Rev. Lett.* **78**, 1335-1338 (1997).
- 29 Murakawa, H. *et al.* Detection of Berry's Phase in a Bulk Rashba Semiconductor. *Science* **342**, 1490-1493 (2013).
- 30 Shcherbakov, D. *et al.* Layer- and gate-tunable spin-orbit coupling in a high-mobility few-layer semiconductor. *Sci. Adv.* **7**, eabe2892 (2021).
- 31 Bihlmayer, G., Noël, P., Vyalikh, D. V., Chulkov, E. V. & Manchon, A. Rashba-like physics in condensed matter. *Nat. Rev. Phys.* **4**, 642-659 (2022).

- 32 Liang, Y. *et al.* Molecular Beam Epitaxy and Electronic Structure of Atomically Thin Oxy-selenide Films. *Adv. Mater.* **31**, 1901964 (2019).
- 33 Zhou, X. *et al.* Step-Climbing Epitaxy of Layered Materials with Giant Out-of-Plane Lattice Mismatch. *Adv. Mater.* **34**, 2202754 (2022).
- 34 Baugher, B. W. H., Churchill, H. O. H., Yang, Y. & Jarillo-Herrero, P. Intrinsic Electronic Transport Properties of High-Quality Monolayer and Bilayer MoS₂. *Nano Lett.* **13**, 4212-4216 (2013).
- 35 Neal, A. T., Liu, H., Gu, J. & Ye, P. D. Magneto-transport in MoS₂: Phase Coherence, Spin–Orbit Scattering, and the Hall Factor. *ACS Nano* **7**, 7077-7082 (2013).
- 36 Radisavljevic, B. & Kis, A. Mobility engineering and a metal–insulator transition in monolayer MoS₂. *Nat. Mater.* **12**, 815-820 (2013).
- 37 Li, L. *et al.* Short and Long Pulse High Magnetic Field Facility at the Wuhan National High Magnetic Field Center. *IEEE Trans. Appl. Supercon.* **24**, 1-4 (2014).
- 38 Xie, J. *et al.* Realisation of the reconfigurable pulsed high magnetic field facility and its scientific application at Wuhan National Pulsed High Magnetic Field Centre. *High Volt.* 1-9 (2023). <https://doi.org/10.1049/hve2.12330>.
- 39 Tan, C. *et al.* Strain-Free Layered Semiconductors for 2D Transistors with On-State Current Density Exceeding 1.3 mA μm^{-1} . *Nano Lett.* **22**, 3770-3776 (2022).
- 40 Zhang, C. *et al.* Single-crystalline van der Waals layered dielectric with high dielectric constant. *Nat. Mater.* **22**, 832-837 (2023).
- 41 Luo, J., Munekata, H., Fang, F. F. & Stiles, P. J. Effects of inversion asymmetry on electron energy band structures in GaSb/InAs/GaSb quantum wells. *Phys. Rev. B* **41**, 7685-7693 (1990).
- 42 Schäpers, T. *et al.* Effect of the heterointerface on the spin splitting in modulation doped In_xGa_{1-x}As/InP quantum wells for B→0. *J. Appl. Phys.* **83**, 4324-4333 (1998).
- 43 Schmult, S. *et al.* Large Bychkov-Rashba spin-orbit coupling in high-mobility GaN/Al_xGa_{1-x}N heterostructures. *Phys. Rev. B* **74**, 033302 (2006).
- 44 Caviglia, A. D. *et al.* Tunable Rashba Spin-Orbit Interaction at Oxide Interfaces. *Phys. Rev. Lett.* **104**, 126803 (2010).
- 45 Fête, A. *et al.* Large modulation of the Shubnikov–de Haas oscillations by the Rashba interaction at the LaAlO₃/SrTiO₃ interface. *New J. Phys.* **16**, 112002 (2014).

- 46 Veit, M. J., Arras, R., Ramshaw, B. J., Pentcheva, R. & Suzuki, Y. Nonzero Berry phase in quantum oscillations from giant Rashba-type spin splitting in LaTiO₃/SrTiO₃ heterostructures. *Nat. Commun.* **9**, 1458 (2018).
- 47 Murakami, S., Nagaosa, N. & Zhang, S.-C. Dissipationless Quantum Spin Current at Room Temperature. *Science* **301**, 1348-1351 (2003).
- 48 Sinova, J. *et al.* Universal Intrinsic Spin Hall Effect. *Phys. Rev. Lett.* **92**, 126603 (2004).
- 49 Xiao, D., Chang, M.-C. & Niu, Q. Berry phase effects on electronic properties. *Rev. Mod. Phys.* **82**, 1959-2007 (2010).
- 50 Ganichev, S. D. *et al.* Spin-galvanic effect. *Nature* **417**, 153-156 (2002).
- 51 Chappert, C., Fert, A. & Van Dau, F. N. The emergence of spin electronics in data storage. *Nat. Mater.* **6**, 813-823 (2007).
- 52 Mihai Miron, I. *et al.* Current-driven spin torque induced by the Rashba effect in a ferromagnetic metal layer. *Nat. Mater.* **9**, 230-234 (2010).
- 53 Su, W. P., Schrieffer, J. R. & Heeger, A. J. Solitons in Polyacetylene. *Phys. Rev. Lett.* **42**, 1698-1701 (1979).
- 54 Wu, J. *et al.* Chemical Patterning of High-Mobility Semiconducting 2D Bi₂O₂Se Crystals for Integrated Optoelectronic Devices. *Adv. Mater.* **29**, 1704060 (2017).

Acknowledgments: We acknowledge Molecular Materials and Nanofabrication Laboratory (MMNL) in the College of Chemistry at Peking University for the use of instruments. This work was supported by the National Key Research and Development Program of China (2022YFA1204900, 2021YFA1202901), the National Natural Science Foundation of China (21920102004, 51861145201, 92164205, 52021006, 22205011, 52072168, 21733001 and 22105009), Beijing National Laboratory for Molecular Sciences (BNLMS-CXTD-202001), and the Tencent Foundation (The XPLOER PRIZE). J.W. acknowledges the support from the Boya Postdoctoral Fellowship.

Author contributions:

H.P., H.Y. and B.Y. conceived the original idea for the project. X.Z., C.T., Y. L. and X.C. synthesized the materials. J.W., X.Z., X.C. and Y.Z. fabricated the devices. X.Z. X.G., R.Z. and P.

G. carried out STEM measurements. J.W. and J.H. carried out static magnetic field transport measurements. Pulsed magnetic field transport measurements were performed by J.W., J.H. and C.T. with the help from J.Z., G.J., H.Z. and Z.Z.. D.K., A.S. and B.Y. carried out theoretical calculations. J.W., J.H., X.Z., A.S., H.P., B.Y., and H.Y. wrote the manuscript. All authors contributed to the scientific planning and discussions.

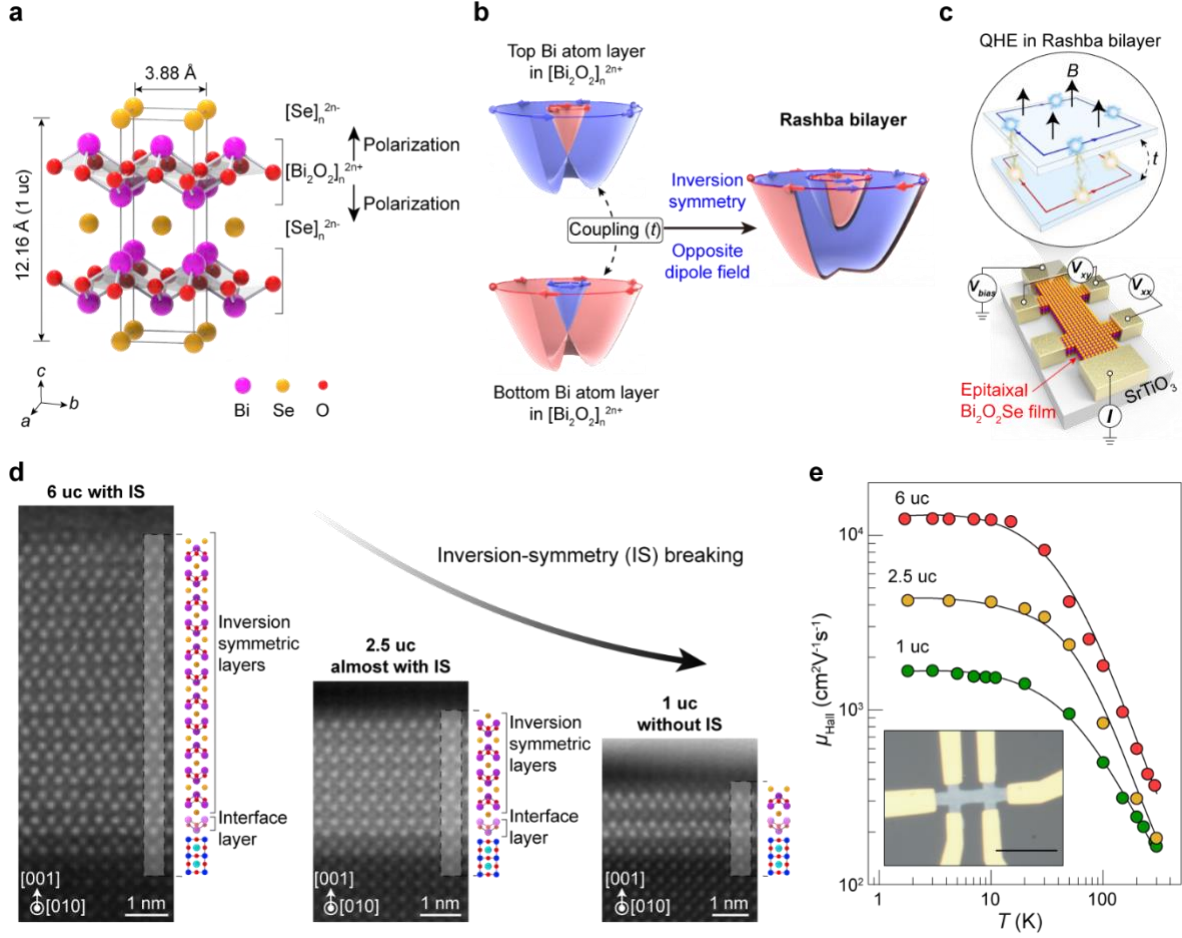


Fig. 1. Rashba bilayer and basic electric characterization of Bi₂O₂Se films. (a) Layered crystal structure of 1 unit cell Bi₂O₂Se with tetragonal [Bi₂O₂]_n²ⁿ⁺ layers and [Se]_n²ⁿ⁻ layers alternately stacked along the *c* axis. (b) In [Bi₂O₂]_n²ⁿ⁺ layers, each Bi monolayer feels a strong Rashba effect while neighboring Bi monolayer exhibits opposite sign in Rashba SOC, resulting in a hidden Rashba effect as well as unique QHE. The bands in different colors represent bands with different spin textures. The arrows stand for the directions of spin. (c) In the schematic view of QHE in Rashba bilayer, electrons in two Rashba layers have different spin textures (colors). (d) Cross-sectional HAADF-STEM image of Bi₂O₂Se films with different thicknesses. The inversion-symmetric layers are plotted in a lighter color. Note: IS represents inversion symmetry. (e) μ_{Hall} as a function of temperature for non-encapsulated Bi₂O₂Se films. The mobility of epitaxial Bi₂O₂Se films reach maximums of $\mu_{\text{Hall}} = 12435, 4230, 1677 \text{ cm}^2 \text{ V}^{-1} \text{ s}^{-1}$ for thicknesses of 6, 2.5 and 1 uc. Inset shows the optical image of a typical Hall bar device for an epitaxial Bi₂O₂Se film. Scale bar: 10 μm.

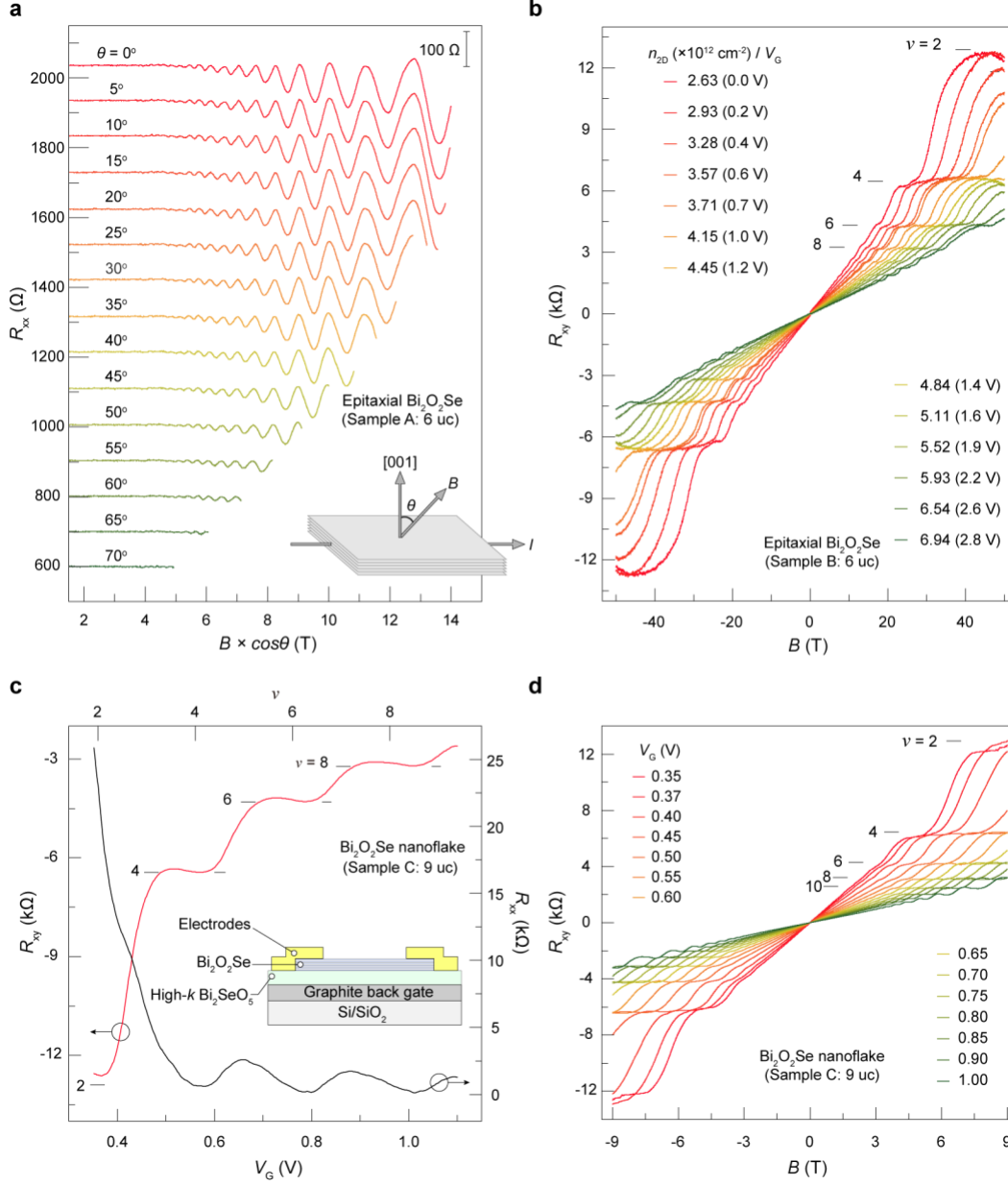


Fig. 2. Absence of odd-integer QHE in the epitaxial $\text{Bi}_2\text{O}_2\text{Se}$ films and $\text{Bi}_2\text{O}_2\text{Se}$ nanosheet. (a) Angle-dependent magnetoresistance as a function of effective magnetic fields ($B_\perp = B \times \cos\theta$). Here, θ is the angle between the magnetic field and the normal direction of the sample plane, as depicted in the inset. The curves are shifted by 100Ω vertically. The positions of the SdH oscillation extrema correspond to unchanged B_\perp under different θ . (b) Hall resistance as a function of the magnetic field measured at varying electron densities in the 6-uc-thick device. The sample was immersed in liquid helium at 4.2 K when applying the pulsed magnetic field up to 50 T. The horizontal lines indicate the resistance related to different even-integer filling factors. (c) Hall resistance and longitudinal resistance as a function of gate voltage at a certain magnetic field $B = 9 \text{ T}$. Quantum Hall plateaus are clearly observed with filling factors ranging from $\nu = 2$ to $\nu = 8$ in a 9-uc-thick free-standing $\text{Bi}_2\text{O}_2\text{Se}$ nanosheet. Inset: schematic of a back-gate $\text{Bi}_2\text{O}_2\text{Se}$ Hall bar device on high- κ Bi_2SeO_5 nanosheet. (d) Hall resistance as a function of magnetic field. Quantum Hall plateaus are clearly observed with ν ranging from 2 to 10.

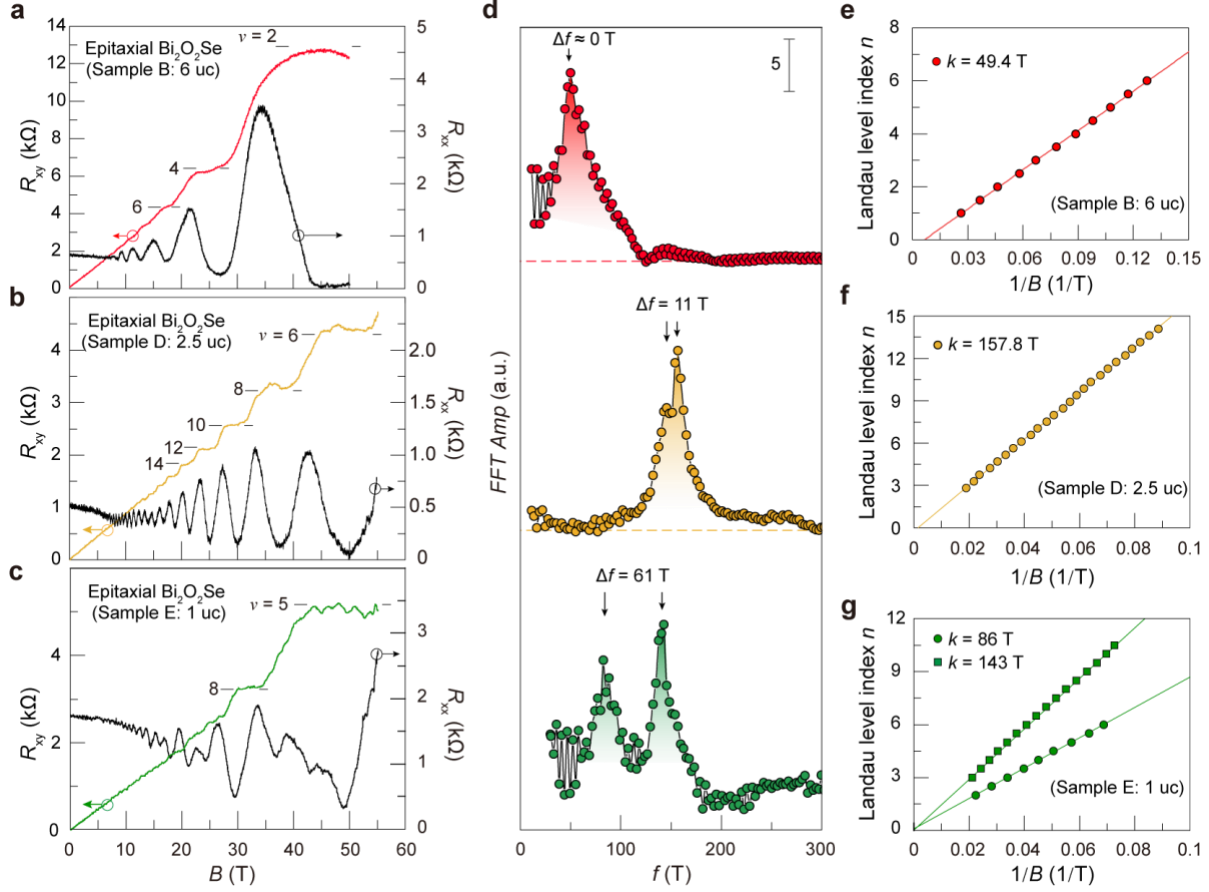


Fig. 3. Thickness-dependent QHE and quantum oscillations in epitaxial $\text{Bi}_2\text{O}_2\text{Se}$ films. (a) Even-integer QHE in the 6-uc-thick sample at 4.2 K. R_{xx} decreases to 0 when $B > 42$ T. (b) Even-integer QHE in the 2.5-uc-thick sample at 4.2 K. The plateau of R_{xy} at $\nu = 6$ corresponds to the position where R_{xx} decreases to almost 0. (c) QHE in the 1-uc-thick sample at 4.2 K. R_{xy} shows quantized plateaus with both even and odd filling factors. (d) FFT analysis of SdH oscillations in 6-, 2.5- and 1-uc-thick devices. (e) Landau plots for the SdH oscillations in (a). To construct the Landau fan diagram, the resistance R_{xx} and R_{xy} was firstly converted into conductance with the anisotropic Hall tensor, and then valleys of conductance are assigned with integers while the peaks are assigned with half integers. (f) Landau plots for the SdH oscillations in the 2.5-uc-thick device. (g) Landau plots in the 1-uc-thick device. Two Landau fans originate from the two splitting peaks in the lowest panel in (d).

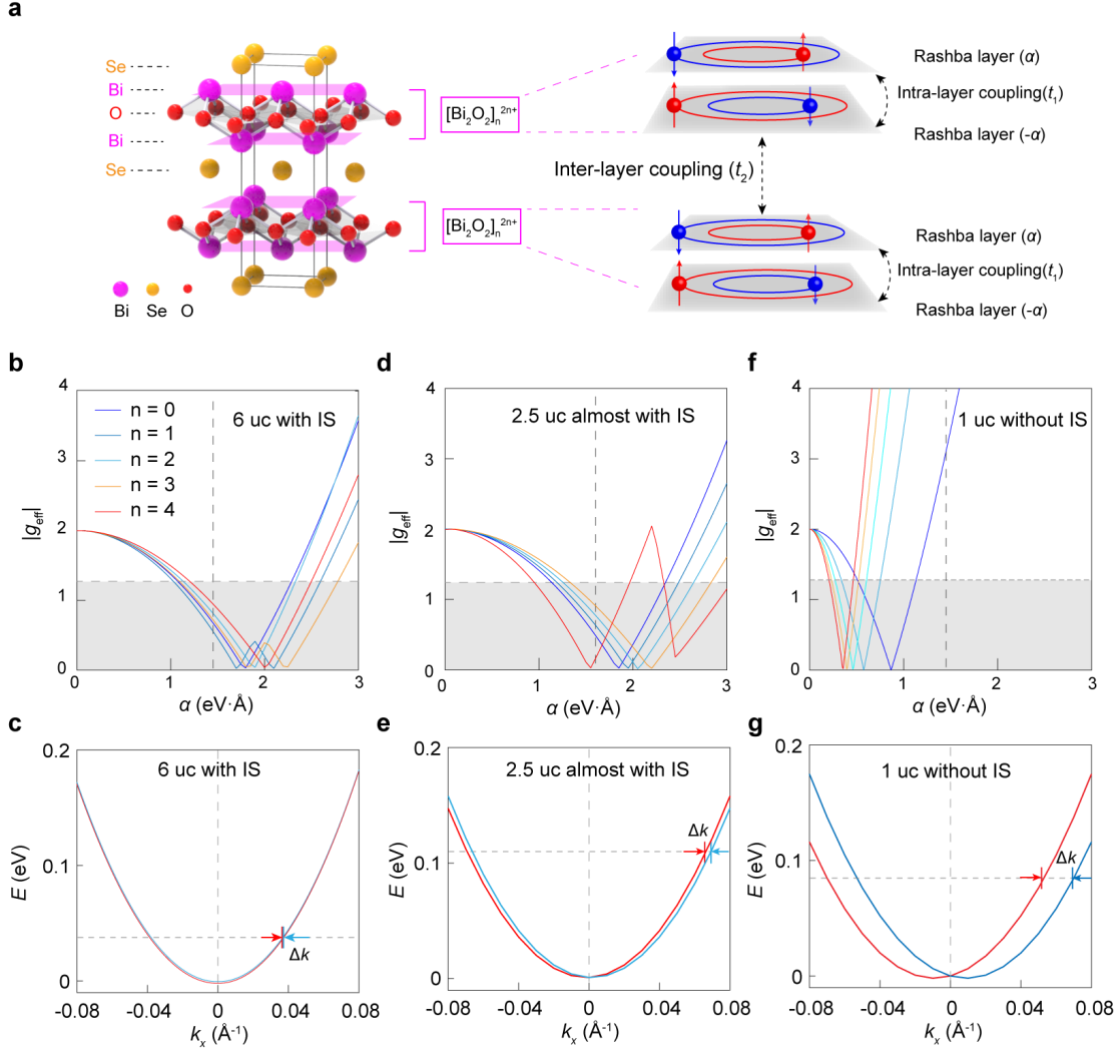


Fig. 4. The calculated effective g -factors and band structures for Bi₂O₂Se thin films. (a) Unit cell of bulk Bi₂O₂Se composed Bi-O layers with alternating spin orbital coupling($\alpha, -\alpha, \alpha, -\alpha$). Each bilayer is inversion-symmetric. The intra-layer coupling is denoted by t_1 while the inter-layer coupling is t_2 . (b), (d), (f) The g_{eff} dependence on α for different films. The vertical dashed line indicates the α value in materials. The horizontal dashed line indicates the upper limit of $g_{eff} = 1.28$ to suppress the Zeeman splitting. Note: IS represents inversion symmetry. (c), (e), (g) Lowest energy band structures for epitaxial Bi₂O₂Se films with different thicknesses, which were derived from the experiments and *ab initio* calculations. The separation between two arrows represents the difference of wave vector due to Rashba splitting, which increases when reducing the film thickness. Lines in different colors represent bands with different spin directions.